



Ferroptosis occurs through an osmotic mechanism and propagates independently of cell rupture

Michelle Riegman^{1,2}, Liran Sagie³, Chen Galed³, Tom Levin³, Noah Steinberg², Scott J. Dixon⁴, Ulrich Wiesner⁵, Michelle S. Bradbury^{1,6,7}, Philipp Niethammer^{1,2}, Assaf Zaritsky³✉ and Michael Overholtzer^{1,2}✉

Ferroptosis is a regulated form of necrotic cell death that is caused by the accumulation of oxidized phospholipids, leading to membrane damage and cell lysis^{1,2}. Although other types of necrotic death such as pyroptosis and necroptosis are mediated by active mechanisms of execution^{3–6}, ferroptosis is thought to result from the accumulation of unrepaired cell damage¹. Previous studies have suggested that ferroptosis has the ability to spread through cell populations in a wave-like manner, resulting in a distinct spatiotemporal pattern of cell death^{7,8}. Here we investigate the mechanism of ferroptosis execution and discover that ferroptotic cell rupture is mediated by plasma membrane pores, similarly to cell lysis in pyroptosis and necroptosis^{3,4}. We further find that intercellular propagation of death occurs following treatment with some ferroptosis-inducing agents, including erastin^{2,9} and C' dot nanoparticles⁸, but not upon direct inhibition of the ferroptosis-inhibiting enzyme glutathione peroxidase 4 (GPX4)¹⁰. Propagation of a ferroptosis-inducing signal occurs upstream of cell rupture and involves the spreading of a cell swelling effect through cell populations in a lipid peroxide- and iron-dependent manner.

The proper regulation of cell death is important for normal organismal development and the maintenance of tissue homeostasis in adulthood. It was once thought that programmed cell death occurred exclusively through apoptosis, whereas necrotic death resulted only from acute cell stress or injury. However, numerous new cell death modalities have recently been discovered, including programmed forms of necrosis that are regulated by specific and distinct cellular machineries¹¹. One form of regulated necrosis—ferroptosis—involves the iron-dependent accumulation of lipid peroxide species in cell membranes^{1,2}. Under physiological conditions, ferroptosis is prevented by antioxidant enzymes that limit the build-up of oxidized lipids, including glutathione peroxidase 4 (GPX4), which uses glutathione as a cofactor to detoxify peroxidation products¹². Cell death can be triggered by GPX4 inactivation, either through direct inhibition or depletion of cellular glutathione, thereby allowing the accumulation of phospholipid peroxides and cell damage. Recent work has uncovered an additional ferroptosis-preventing mechanism controlled by ferroptosis suppressor protein 1 (FSP1), which catalyses the reduction of the lipophilic antioxidant coenzyme Q10 (CoQ)^{13,14}.

Ferroptosis was previously shown to spread through cell populations, resulting in spatiotemporal patterns of cell death with a wave-like appearance not previously observed in other forms of cell death^{7,8}. It is unknown what mechanism underlies this phenomenon and whether death propagation between neighbouring cells is a consistent feature of ferroptosis or occurs only under certain conditions. Given the emerging links between ferroptosis and degenerative diseases that often involve large, continuous areas of tissue damage, the propagative nature of ferroptosis is important to understand¹⁵. Furthermore, while factors that affect the accumulation of lipid peroxides and thereby modulate ferroptosis have been elucidated^{1,16}, little is known about how lipid peroxidation leads to plasma membrane permeabilization. Whether cell lysis is involved in the intercellular propagation of ferroptosis is also unknown¹⁷. Here, we investigate the wave-like nature of ferroptosis, the mechanism of ferroptotic cell rupture and the link between the two processes.

We previously observed wave-like spreading of ferroptosis when cells were treated with ferroptosis-inducing nanoparticles called C' dots (Fig. 1a,b and Supplementary Video 1)⁸, and a similar phenomenon has been reported in mouse renal tubules treated with the ferroptosis-inducing agent erastin⁷. However, the spatiotemporal patterns of ferroptosis have not been investigated systematically¹⁵. To quantitatively study propagation, we performed live-cell imaging of several cell lines (MCF10A mammary epithelium, MCF7 breast cancer, U937 promonocytic leukaemia, HAP1 chronic myelogenous leukaemia and B16F10 melanoma) in the presence of the cell death indicator SYTOX Green and different ferroptosis-inducing agents (C' dots⁸, erastin², the GPX4 inhibitor ML162^{10,18} or a combination of ferric ammonium citrate (FAC) and buthionine sulfoxamine (BSO); Extended Data Fig. 1a,b). We then used a bootstrapping approach to quantify potential non-random patterns of cell death. For each video, we calculated the mean time difference between neighbouring cell deaths, $\mu_{\text{exp}\Delta t}$, and compared this experimental value to a distribution of means derived from computationally generated permutations representing random orders of death (Fig. 1c,d). Consistent with wave-like propagation, ferroptosis occurred with non-random spatiotemporal patterns when it was induced by erastin, C' dots or FAC and BSO, as determined by comparing $\mu_{\text{exp}\Delta t}$ to the 95th percentile of the random distribution, $\mu_{\text{perm}95\Delta t}$ (Fig. 1b,d,g and Extended Data Fig. 1c). Interestingly, when ferroptosis was induced by inhibition of GPX4 through treatment

¹Louis V. Gerstner, Jr. Graduate School of Biomedical Sciences, Memorial Sloan Kettering Cancer Center, New York, NY, USA. ²Cell Biology Program, Sloan Kettering Institute for Cancer Research, New York, NY, USA. ³Department of Software and Information Systems Engineering, Ben-Gurion University of the Negev, Beer-Sheva, Israel. ⁴Department of Biology, Stanford University, Stanford, CA, USA. ⁵Department of Materials Science & Engineering, Cornell University, Ithaca, NY, USA. ⁶Department of Radiology, Sloan Kettering Institute for Cancer Research, New York, NY, USA. ⁷Molecular Pharmacology Program, Sloan Kettering Institute for Cancer Research, New York, NY, USA. ✉e-mail: assafza@bgu.ac.il; overholm1@mskcc.org

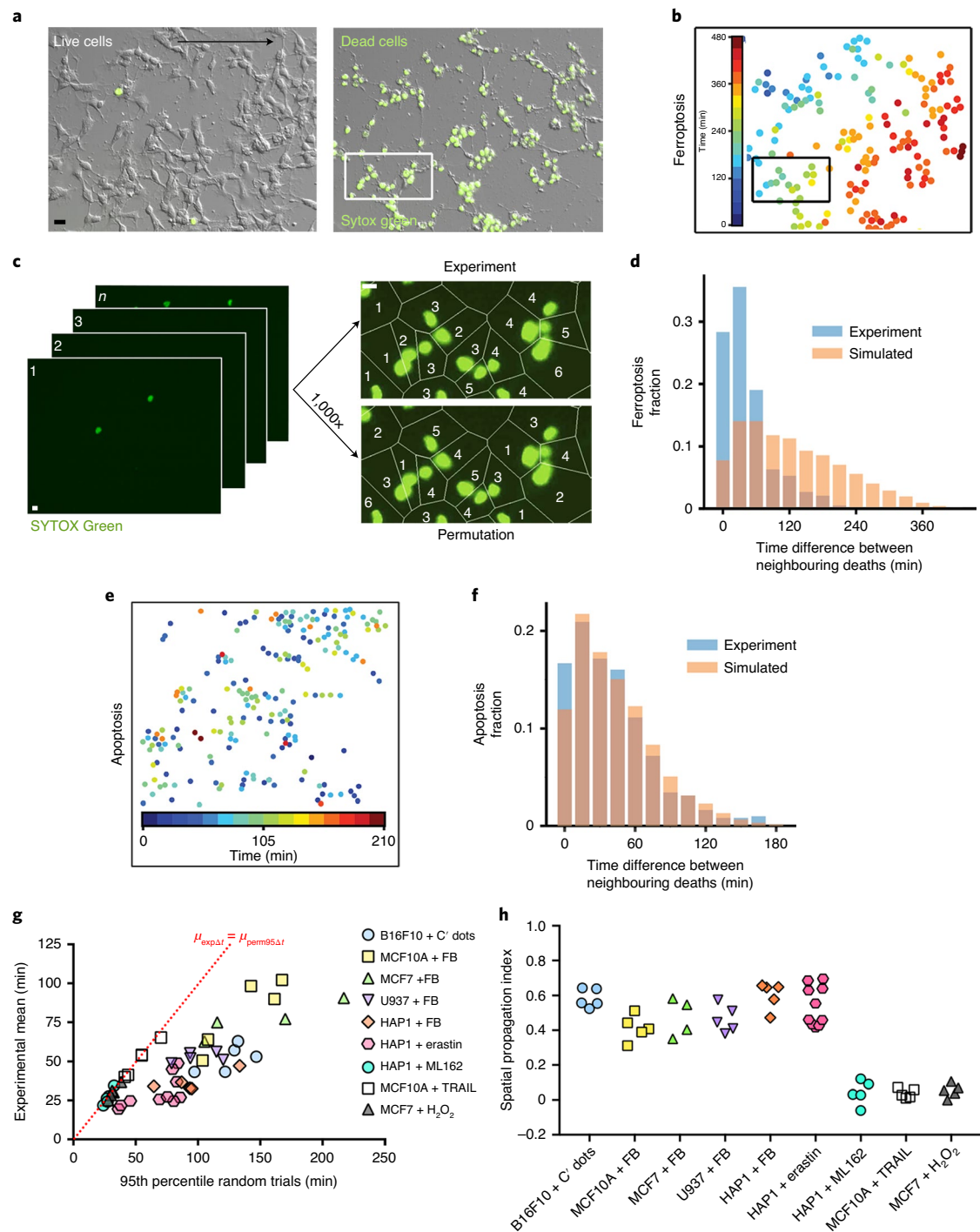


Fig. 1 | Ferroptosis exhibits propagative spatiotemporal patterns. **a**, B16F10 cells treated with C' dot nanoparticles in amino acid-free (–AA) medium to induce ferroptosis. Images: differential interference contrast (DIC) (left) and SYTOX Green (right). SYTOX-positive cells are dead. Scale bar, 20 μm . Images are representative of five videos from one experiment. **b**, Nuclei of ferroptotic cells in **a**, pseudocoloured to indicate the relative timing of cell death, as determined by time-lapse microscopy (Supplementary Video 1). **c**, Schematic summarizing our method to quantify cell death patterns. Images from time-lapse microscopy (left) are processed to determine the relative timing of neighbouring cell deaths (top right image, 'experiment') versus permuted trials (bottom right image, 'permutation') to detect potential non-random patterns. The images match the boxed areas in **a** and **b**. Scale bar, 10 μm . **d**, Distribution of time differences between neighbouring deaths (Δt) from the experiment in **a–c** (blue) versus the averaged distribution of the set of random permutations (orange). The graph shows the fraction of total deaths for the given time differences. **e**, Spatiotemporal distribution of apoptosis in MCF10A cells treated with TRAIL. Each dot represents a cell; colours indicate relative times of cell death as determined by cell morphology. Data are representative of five fields of view from one experiment. **f**, Distribution of experimental time differences between neighbouring deaths (Δt) (blue) and averaged distribution of Δt values from the corresponding permuted data in orange. Data belong to the experiment shown in **e**. **g**, Ferroptosis, apoptosis and H_2O_2 -induced necrosis show non-random spatiotemporal patterns. $\mu_{\text{exp}\Delta t}$ is shown versus $\mu_{\text{perm}95\Delta t}$ of different cell lines undergoing ferroptosis induced by the indicated treatment (FB = FAC + BSO), apoptosis induced with TRAIL or necrosis induced with H_2O_2 . The dashed line indicates $\mu_{\text{exp}\Delta t} = \mu_{\text{perm}95\Delta t}$. Each data point represents one video. Data are from two independent experiments for MCF7 + H_2O_2 and one experiment for all other conditions. **h**, The spatial propagation index generated from data in **g**.

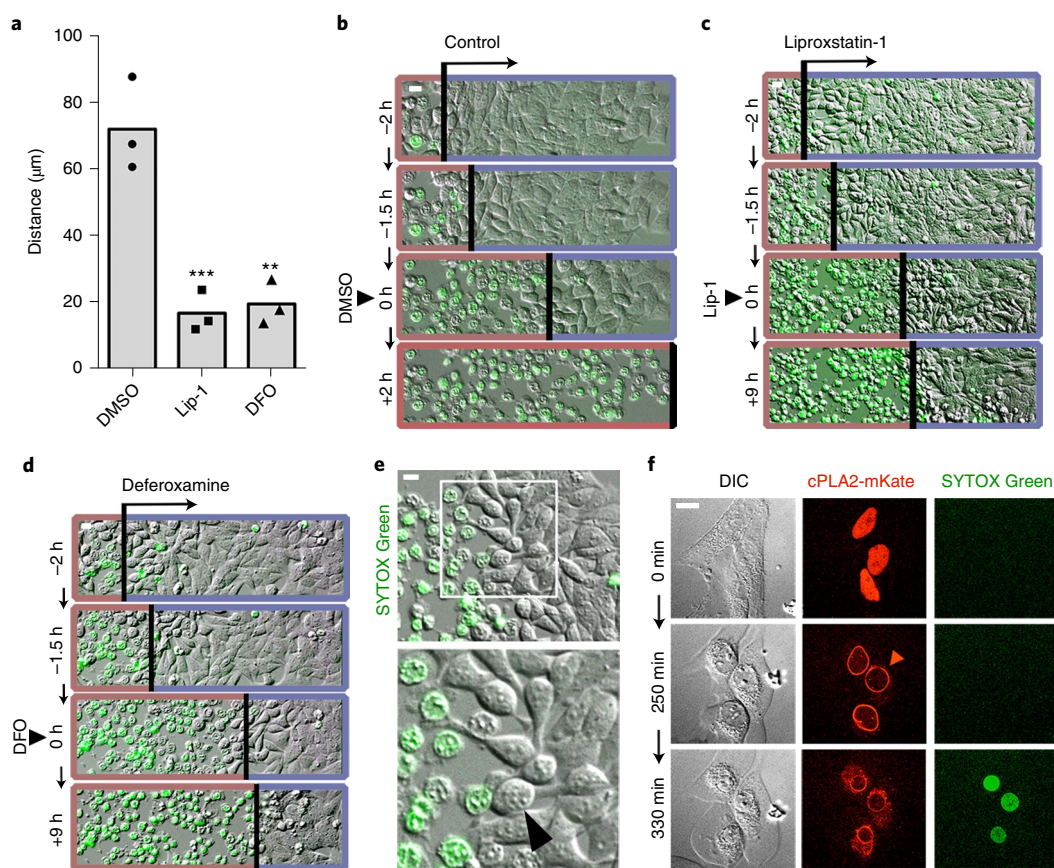


Fig. 2 | Ferroptosis spreading requires lipid peroxidation and iron and involves cell swelling. **a**, Distance of ferroptosis spreading in HAP1 cells incubated with FAC and BSO, and treated with liproxstatin-1 (Lip-1), deferoxamine (DFO) or DMSO control after wave initiation. Distance was quantified 2 h after drug addition. $N=3$ independent experiments, averaged across three or four microscopic fields of view per replicate. Dunnett's test; $***P=0.0008$, $**P=0.001$. **b–d**, Representative images from the experiments quantified in **a**. The time of treatment with DMSO (**b**), Lip-1 (**c**) or DFO (**d**) is indicated as 0 h. Images show DIC and SYTOX Green fluorescence. Death waves are indicated by an arrow and a red border; live cells are indicated with a blue border on each image. Note that Lip-1- and DFO-treated cells are shown 9 h after treatment (+9 h), versus 2 h after treatment for DMSO (+2 h). See Supplementary Video 3. **e**, HAP1 cells treated with FAC and BSO are round before ferroptotic cell rupture (arrowhead). Images are representative of four independent experiments. **f**, The cell swelling marker cPLA2-mKate translocates to the nuclear envelope (arrowhead) before SYTOX Green labelling in HeLa cells treated with FAC and BSO (Supplementary Video 4). Images are representative of two independent experiments. All scale bars, 10 μm. Statistical source data are provided in Source Data Fig. 2.

with ML162, $\mu_{\text{exp}\Delta t}$ was more similar to the 95th percentile of the random permutations (Fig. 1g and Extended Data Fig. 1d,e).

To measure intercellular death propagation in different forms of cell death, we induced necrosis by treatment with hydrogen peroxide (H_2O_2) and apoptosis using tumour necrosis factor-related apoptosis-inducing ligand (TRAIL). Although H_2O_2 -induced necrosis and TRAIL-induced apoptosis displayed no visually obvious wave-like spreading of death (Fig. 1e,f and Supplementary Video 2), they did result in death patterns with non-random spatiotemporal features (Fig. 1g). To better compare the propagative features of these different forms of cell death, we devised a measure termed the spatial propagation index (SPI). When propagation is not the major determinant of the spatiotemporal distribution of cell death across a population, we expect $\mu_{\text{exp}\Delta t}$ to have similar or larger values than $\mu_{\text{perm}95\Delta t}$, as death occurs independently of neighbouring cell deaths in the vicinity. However, when propagation does play a major role—that is, cells are affected by the death of their neighbours—we expect $\mu_{\text{exp}\Delta t}$ to be much smaller than $\mu_{\text{perm}95\Delta t}$ due to the non-random spatial order of death. Thus we defined

$$\text{SPI} = \frac{\mu_{\text{perm}95\Delta t} - \mu_{\text{exp}\Delta t}}{\mu_{\text{perm}95\Delta t}}$$

which is the spatial contribution to the observed death patterns as a fraction of the neighbouring death times expected if death order were spatially random. The SPI indicates that cell death propagation plays a dominant role when ferroptosis is induced by erastin, C' dots or FAC and BSO, but not when induced by ML162 (Fig. 1h). Similarly, H_2O_2 -induced necrosis and TRAIL-induced apoptosis also do not exhibit propagative features (Fig. 1h). These results demonstrate that the ability to spread in wave-like patterns by propagating between neighbouring cells is a feature of particular forms of ferroptosis.

To examine the mechanism of ferroptotic propagation, we first asked whether iron and lipid peroxidation, two known drivers of ferroptosis, are required for propagation. The addition of the lipid peroxidation inhibitor liproxstatin-1 or the iron chelator deferoxamine (DFO) to cell cultures after the initiation of ferroptosis stopped death from spreading (Fig. 2a–d and Supplementary Video 3), demonstrating that iron and lipid peroxidation are both required for continuous ferroptosis propagation. Because iron and lipid peroxidation are also necessary for ferroptosis to occur in individual cells, these results suggested that the full execution of ferroptosis, including cell lysis, could be required for the spreading of death between cells.

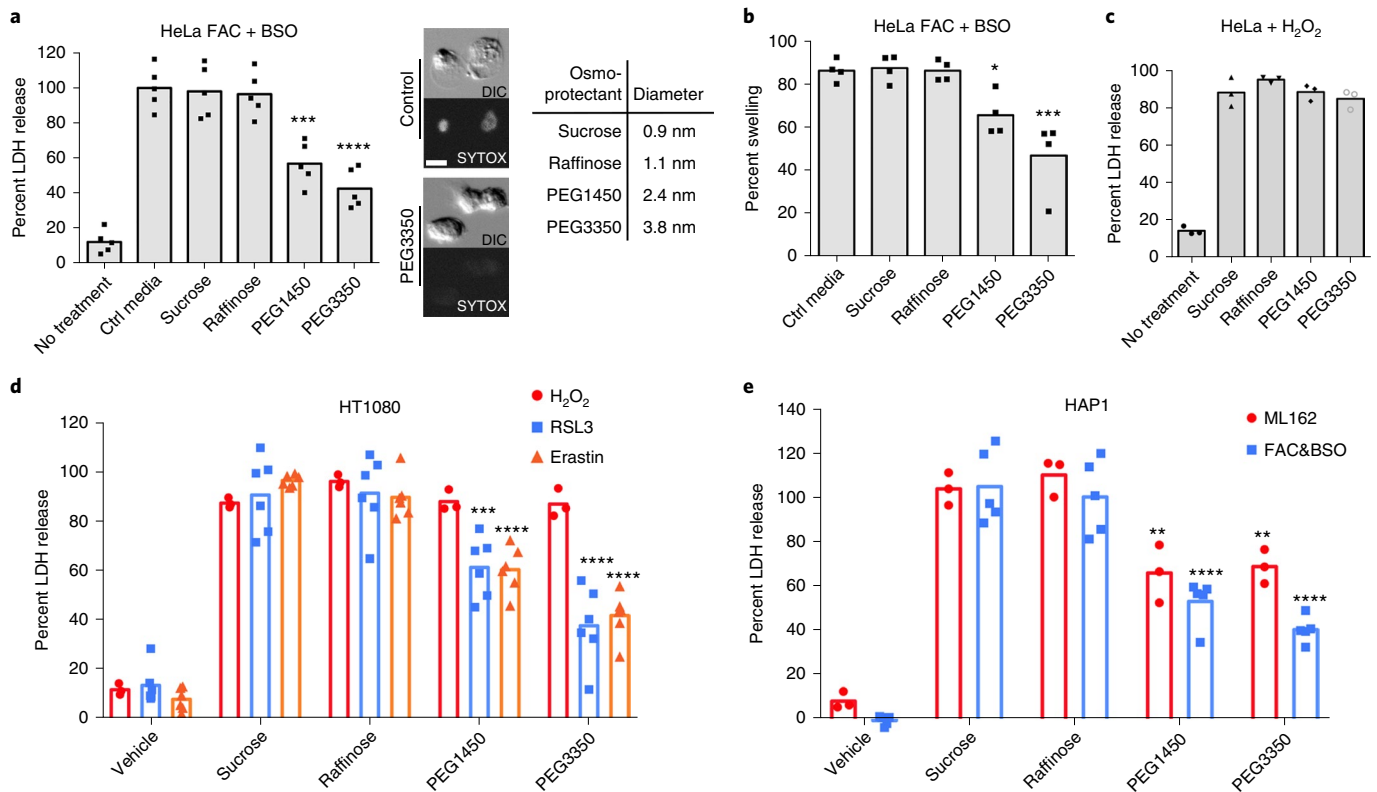


Fig. 3 | Ferroptotic cell rupture is inhibited by osmoprotectants. a, Percent LDH released from ferroptotic HeLa cells treated with FAC and BSO and the indicated osmoprotectants: sucrose, raffinose, PEG1450 and PEG3350. Images show DIC and SYTOX Green fluorescence for HeLa cells treated with FAC + BSO in the presence or absence of PEG3350. Scale bar, 10 μ m. The diameters of the osmoprotectants are shown in the table. $N = 5$ biologically independent experiments. Dunnett's test; $***P = 0.0001$, $****P = 0.0001$. **b**, Swelling of ferroptotic HeLa cells treated with FAC and BSO as measured by recruitment of cPLA2-mKate to the nuclear envelope, determined by time-lapse microscopy. $N = 4$ biologically independent experiments. Dunnett's test; $*P = 0.0318$, $***P = 0.0002$. **c**, LDH release by HeLa cells treated with H_2O_2 and the indicated osmoprotectants, relative to HeLa cells treated with H_2O_2 only. $N = 3$ biologically independent experiments. Dunnett's test; all comparisons not significant. Raffinose, $P = 0.307$; PEG1450, $P = 0.9999$; PEG3350, $P = 0.7764$. **d,e**, LDH release in HT1080 cells treated with H_2O_2 , RSL3 or erastin (**d**) and HAP1 cells treated with ML162 or FAC and BSO and the indicated osmoprotectants (**e**), relative to the treatment alone. $N = 6$ (RSL3 and erastin), 3 (H_2O_2 and ML162) or 5 (FAC + BSO) biologically independent experiments. Dunnett's test: RSL3 + PEG1450, $P = 0.0067$; erastin + PEG1450, $P = 0.0001$; RSL3 + PEG3350, $P = 0.0001$; erastin + PEG3350, $P = 0.0001$; ML162 + PEG1450, $P = 0.003$; FAC&BSO + PEG1450, $P = 0.0001$; ML162 + PEG3350, $P = 0.0048$; FAC&BSO + PEG3350, $P = 0.0001$. Statistical source data are provided in Source Data Fig. 3.

How ferroptosis is executed downstream of lipid peroxidation is not clearly defined. We noted from time-lapse imaging that ferroptotic cells appeared to round and swell before cell death (Fig. 2e). Like cell death, swelling also appeared to spread through cell populations in a manner that was blocked by treatment with liproxstatin-1 or DFO (Supplementary Video 3). Expression of an mKate-tagged version of the zebrafish cPLA2 enzyme, which localizes to the nuclear envelope upon osmotic swelling in HeLa cells¹⁹, confirmed that ferroptotic cells indeed swell prior to undergoing rupture (Fig. 2f and Supplementary Video 4). Cell swelling is also known to occur during pyroptosis and necroptosis, both of which involve the formation of pores in the plasma membrane, leading to the influx of extracellular ions and water molecules^{3,4}. Pore-mediated cell rupture can be inhibited by incubating cells with large carbohydrates known as osmoprotectants⁴. Osmoprotectants with a diameter larger than the pores protect cells from lysis by osmotically balancing large intracellular molecules that cannot diffuse freely across the perforated membrane, while smaller osmoprotectants do not. Thus, although osmoprotectants of sufficient size do not block plasma membrane permeabilization, pore-mediated ion exchange or cell death, they prevent osmotic cell lysis caused by pore formation. Indeed, cell rupture resulting from FAC and BSO-induced ferroptosis, as measured by the release of lactate dehydrogenase (LDH), was inhibited by the

addition of polyethylene glycols (PEGs) with molecular weights of 1,450 and 3,350 Da (PEG1450 and PEG3350), but not by the smaller osmoprotectants sucrose and raffinose (Fig. 3a). The translocation of cPLA2-mKate to the nuclear envelope was also reduced by PEG1450 and PEG3350 (Fig. 3b), suggesting that ferroptotic swelling and rupture may be caused by the opening of nanoscale pores in the plasma membrane. Induction of ferroptosis with erastin or the GPX4 inhibitors RSL3 and ML162 likewise resulted in cell rupture that was inhibited by treatment with PEG1450 or PEG3350 (Fig. 3d,e). LDH release caused by H_2O_2 -induced death, on the other hand, was not affected by osmoprotectants (Fig. 3c,d).

As ferroptotic cell rupture could be inhibited using osmoprotectants, we sought to examine whether cell lysis is required for ferroptosis propagation. When HAP1 cells were treated with FAC and BSO in the presence of the osmoprotectant PEG1450, we observed waves of cell rounding that spread through cell colonies and appeared similar to waves of cell death (Supplementary Video 5). However, SYTOX uptake was reduced, consistent with the inhibition of cell rupture. To quantify these waves, we expressed a fluorescent sensor of nuclear calcium (GCaMP6-NLS) in HAP1 cells, reasoning that pore formation might lead to a spike in intracellular calcium levels that could be used as a readout of cell permeabilization. Live imaging of ferroptotic cells demonstrated that GCaMP fluorescence

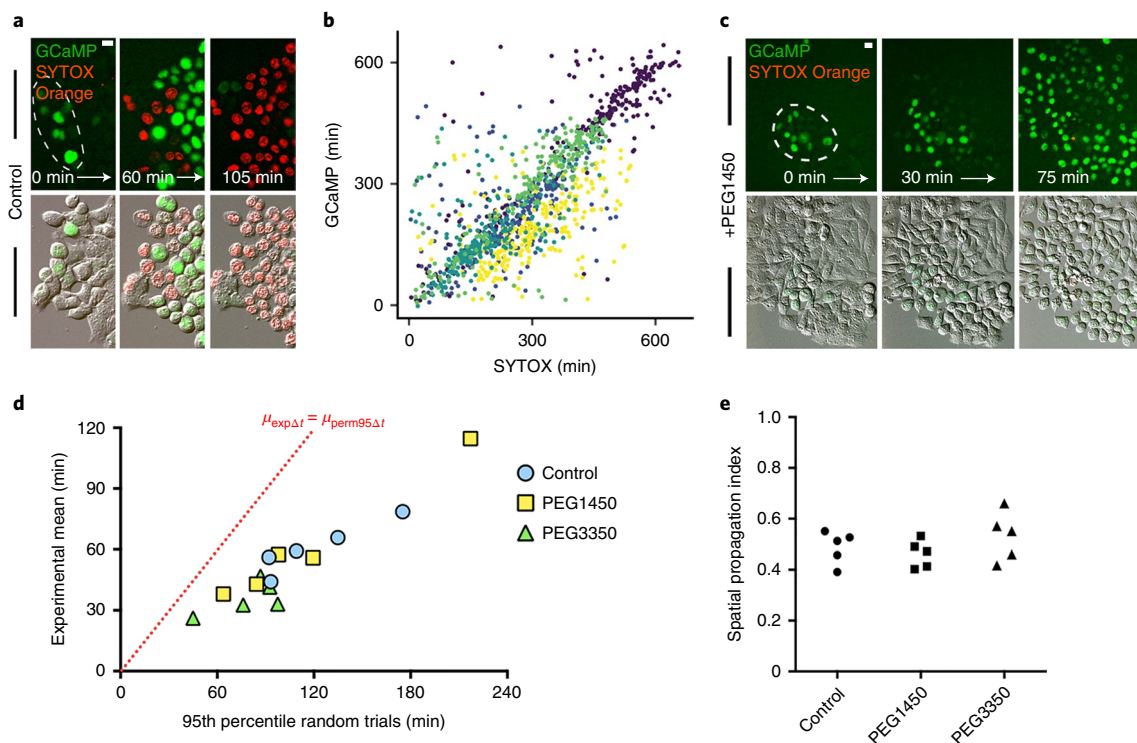


Fig. 4 | Ferroptosis spreading involves calcium flux and does not require cell rupture. a, Images show spreading of GCaMP fluorescence (green) before cell rupture marked by SYTOX Orange (red) in HAP1 cells treated with FAC and BSO. The dashed oval shows the origin of death spreading. Note that cells lose GCaMP fluorescence upon cell rupture, probably due to GCaMP efflux. See Supplementary Video 6. Images are representative of three independent experiments. **b**, Correlation between relative timing of GCaMP fluorescence and SYTOX labelling in HAP1 cells treated with FAC and BSO and PEG1450. Each dot represents a cell and each colour represents a different field of view. Data are from one experiment. **c**, Images show spreading of GCaMP fluorescence (green) and SYTOX Orange (red) in HAP1 cells treated with FAC and BSO and PEG1450. The dashed oval shows the origin of death spreading. Note that PEG1450-treated cells maintain GCaMP fluorescence and do not label with SYTOX Orange, unlike the control cells in **a**. See Supplementary Video 7. Images are representative of three independent experiments. **d**, Graph showing $\mu_{\text{exp}\Delta t}$ versus $\mu_{\text{perm}95\Delta t}$ of videos of HAP1 cells treated with FAC and BSO and the indicated osmoprotectants, analysed using GCaMP fluorescence. The dashed line indicates $\mu_{\text{exp}\Delta t} = \mu_{\text{perm}95\Delta t}$. Each data point represents one video. Data are from one experiment. **e**, SPI calculated for the experiments shown in **d**. All scale bars, 10 μm . Statistical source data are provided in Source Data Fig. 4.

indeed increased prior to the uptake of SYTOX, and that GCaMP signals spread through cell populations in a similar manner to SYTOX and cell rounding (Fig. 4a and Supplementary Video 6). We compared the relative timing of GCaMP and SYTOX fluorescence for individual cells and found a high degree of correlation, indicating that GCaMP signals could be used instead of SYTOX uptake to assess propagation (Fig. 4b). When cells were treated with PEG1450 to inhibit rupture, wave-like spreading of GCaMP fluorescence still occurred (Fig. 4c and Supplementary Video 7). We quantitatively examined the spatiotemporal GCaMP patterns, and found that their non-random nature was similar to SYTOX death waves in both the presence and absence of osmoprotectants (Fig. 4d,e), demonstrating that propagation occurs in the absence of cell rupture.

Although treatment with osmoprotectants did not prevent propagation, we wondered if it might affect wave speed. To test this we used U937 cells, which exhibit long-lived, unidirectional waves of ferroptosis that can be imaged by differential interference contrast (DIC) microscopy, even in the absence of SYTOX staining (Fig. 5a). Treatment of U937 cells with PEG3350 inhibited cell lysis (Fig. 5b), yet had no effect on the induction of cell death waves (Supplementary Video 8), consistent with the HAP1 data. However, when we measured the speed of these ferroptosis waves, we found them to be slightly but significantly slower in the presence of PEG3350 (1.66 versus 1.37 $\mu\text{m min}^{-1}$; Fig. 5c), demonstrating that ferroptosis propagation is faster when cells are able to fully lyse.

Together, these data indicate that wave-like spreading is a feature of specific forms of ferroptosis that require the continuous presence of iron and lipid peroxidation, and involve a signal that propagates upstream of cell rupture. Although ferroptosis propagation has been observed previously^{7,8}, here we quantitatively establish the existence of non-random spatiotemporal patterns of ferroptosis in multiple contexts. Our method allowed us to distinguish two types of ferroptosis: cell-autonomous or ‘single-cell ferroptosis’, observed in response to GPX4 inhibition, and propagative or ‘multicellular ferroptosis’, which is induced by treatments that inhibit the generation of glutathione (erastin, BSO) and/or increase cellular iron concentrations (FAC, C’ dots). Why direct GPX4 inhibition does not induce propagative ferroptosis is important to examine in future studies, and may relate to activities of iron or functions of glutathione that do not directly involve GPX4²⁰.

Non-autonomous cell death effects have been described elsewhere, most notably in the radiation-induced bystander effect (RIBE), where damage and death rates are increased in cells adjacent to those exposed to radiation²¹. Although RIBE may increase death frequencies, such phenotypes appear distinct from the wave-like death observed during ferroptosis that, in many cases, leads to the near-complete elimination of a cell population^{7,8,15}. Further discovery of the underlying molecular mechanisms is required to determine whether death propagation in these different systems involves similar signalling mechanisms. Numerous factors are proposed to mediate RIBE, including gap junctions, transforming

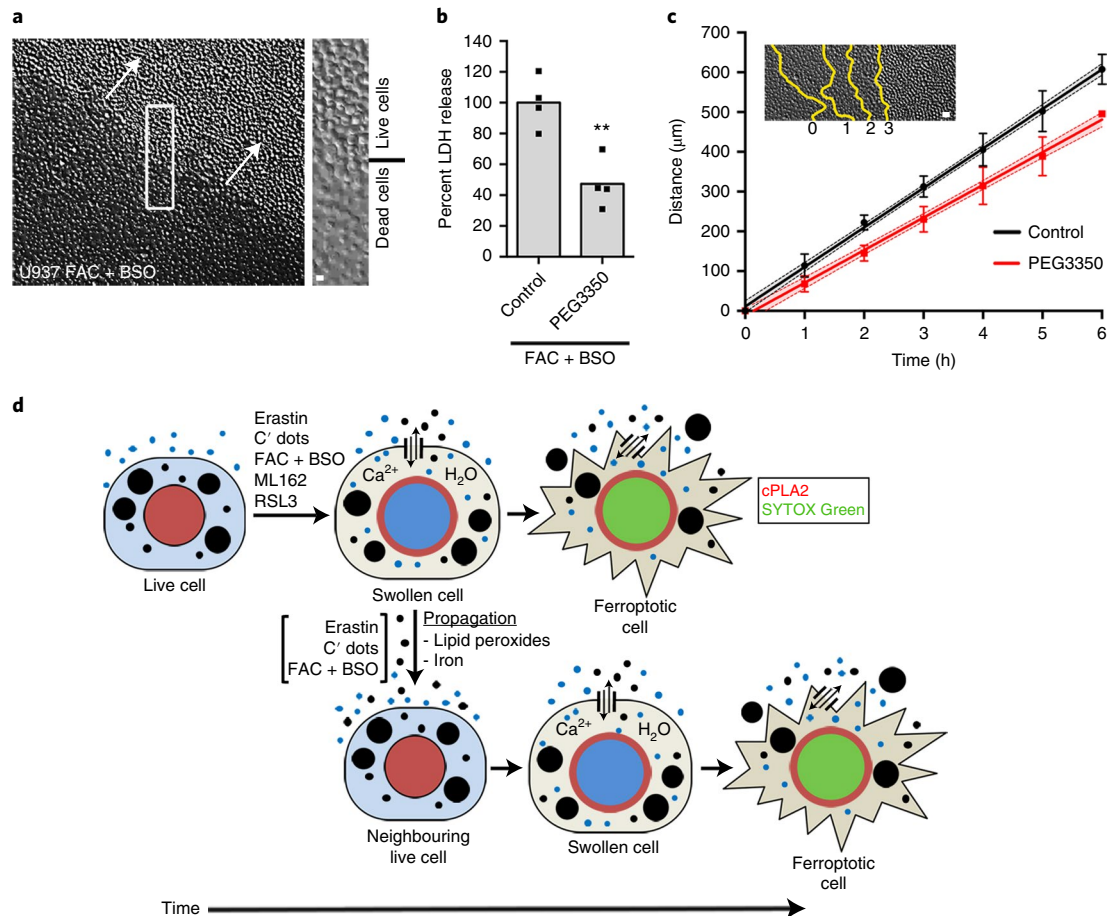


Fig. 5 | PEG3350 slows ferroptosis propagation. **a**, Wave-like spreading of ferroptosis in U937 cells treated with FAC and BSO, imaged by DIC microscopy. Arrows indicate the direction of wave spreading. The image is representative of four independent experiments. Scale bar, 10 μm . Inset: the boundary between live and dead cells. See Supplementary Video 8. **b**, Percent LDH release in U937 cells treated with FAC and BSO in control and PEG3350-treated conditions. Data are from four biological replicates. $**P=0.004$ and was obtained using a two-sided *t*-test. **c**, Wave-like spreading of ferroptosis is slower in the presence of PEG3350. Inset shows a representative example of death progression at each time point indicated by yellow lines. Graph shows distance over time of wave spreading in U937 cells treated with FAC and BSO. Data points indicate means from five independent waves per condition; error bars represent s.d.; line shows linear regression and its 95% confidence interval (shaded regions). Scale bar, 25 μm . **d**, Model for osmotic regulation of ferroptosis and cell death propagation. Ferroptosis induction involves the opening of plasma membrane pores that allow for solute exchange with the external environment, leading to cell swelling that occurs prior to cell death and is marked by cPLA2 translocation to the nuclear membrane (red). After swelling, ferroptotic cells undergo rupture and death marked by the rapid influx of death-indicating dyes such as SYTOX Green. When ferroptosis is induced by treatment with erastin, C' dots, or FAC and BSO, but not by treatment with the GPX4 inhibitor ML162, death propagates to neighbouring cells in an iron- and lipid peroxide-dependent manner, through a signal that is sent independently of cell rupture. Statistical source data are provided at Source Data Fig. 5.

growth factor- β^{22} , p53 and cyclooxygenase-2 signalling²¹. Although our U937 data suggest that gap junctions are not involved in ferroptosis propagation, because these cells do not form cell junctions (Supplementary Video 8), whether other RIBE signals could play a role in ferroptosis spreading is not yet known. Our finding that the presence of an osmoprotectant slows propagation could suggest that the release of a spreadable factor is enhanced by cell rupture, although further experiments are needed to test this.

Our data also indicate that ferroptosis is an osmotic process, as it involves cell swelling (Fig. 5d), and can be blocked by the addition of large osmoprotectants. The ability of osmoprotectants to block lysis following induction of necroptosis or pyroptosis, both in culture and in vivo, and the observed size dependence of the protective effects of different osmoprotectants (Fig. 3), have been interpreted previously as evidence for the existence of pore-like structures that trigger lysis in these forms of necrosis^{3,4}. This is indeed known to occur during pyroptosis, in which the caspase-dependent cleavage

of gasdermin D triggers its oligomerization in the plasma membrane^{23,24}. Similarly, necroptosis may involve plasma membrane permeabilization mediated by the pseudokinase MLKL^{25,26}. Our data thus suggest that ferroptotic rupture is mediated by the formation of plasma membrane pores of a few nanometres in diameter and that cell permeabilization during ferroptosis could be a regulated process. Intriguingly, lipid peroxidation has been proposed to lead to conformational changes in lipid domains and plasma membrane regions^{27,28}, raising the possibility that pore formation could occur through a lipid-based mechanism rather than by activation of a pore-forming protein. Ferroptotic pore formation could regulate not only cell death execution but also the potential release of pro-inflammatory cytokines or DAMPs, which is known to occur during pyroptosis²⁹. We have previously shown that ferroptosis induction in mouse xenografts leads to tumour regression and a concomitant immune response, implying that ferroptosis-inducing agents may be promising cancer therapies^{8,15}. Ferroptosis is also

implicated in cell death resulting from ischaemia reperfusion injury during stroke or myocardial infarction, as well as in acute kidney injury, all of which result in the formation of large zones of necrotic tissue, possibly indicating a role for ferroptosis propagation in these diseases^{1,15}. Intriguingly, the paper by Katikaneni et al. published in this issue shows large waves of cellular deformation occurring in intact zebrafish larvae following microperfusion of arachidonic acid³⁰. As arachidonic acid is a known driver of ferroptosis, this finding suggests that wave-like propagation of ferroptosis may also occur *in vivo*, causing widespread tissue damage³⁰. Uncovering the molecular mechanisms that regulate ferroptosis execution and propagation through cell populations will ultimately further our understanding of how modulators of ferroptosis may be leveraged for therapeutic benefit.

Online content

Any methods, additional references, Nature Research reporting summaries, source data, extended data, supplementary information, acknowledgements, peer review information; details of author contributions and competing interests; and statements of data and code availability are available at <https://doi.org/10.1038/s41556-020-0565-1>.

Received: 28 January 2020; Accepted: 24 July 2020;

Published online: 31 August 2020

References

1. Stockwell, B. R. et al. Ferroptosis: a regulated cell death nexus linking metabolism, redox biology and disease. *Cell* **171**, 273–285 (2017).
2. Dixon, S. J. et al. Ferroptosis: an iron-dependent form of nonapoptotic cell death. *Cell* **149**, 1060–1072 (2012).
3. Ros, U. et al. Necroptosis execution is mediated by plasma membrane nanopores independent of calcium. *Cell Rep.* **19**, 175–187 (2017).
4. Fink, S. L. & Cookson, B. T. Caspase-1-dependent pore formation during pyroptosis leads to osmotic lysis of infected host macrophages. *Cell Microbiol.* **8**, 1812–1825 (2006).
5. Degtarev, A. et al. Chemical inhibitor of nonapoptotic cell death with therapeutic potential for ischemic brain injury. *Nat. Chem. Biol.* **1**, 112–119 (2005).
6. Cookson, B. T. & Brennan, M. A. Pro-inflammatory programmed cell death. *Trends Microbiol.* **9**, 113–114 (2001).
7. Linkermann, A. et al. Synchronized renal tubular cell death involves ferroptosis. *Proc. Natl Acad. Sci. USA* **111**, 16836–16841 (2014).
8. Kim, S. E. et al. Ultrasmall nanoparticles induce ferroptosis in nutrient-deprived cancer cells and suppress tumour growth. *Nat. Nanotechnol.* **11**, 977–985 (2016).
9. Dolma, S., Lessnick, S. L., Hahn, W. C. & Stockwell, B. R. Identification of genotype-selective antitumor agents using synthetic lethal chemical screening in engineered human tumor cells. *Cancer Cell* **3**, 285–296 (2003).
10. Yang, W. S. et al. Regulation of ferroptotic cancer cell death by GPX4. *Cell* **156**, 317–331 (2014).
11. Galluzzi, L. et al. Molecular mechanisms of cell death: recommendations of the Nomenclature Committee on Cell Death 2018. *Cell Death Differ.* **25**, 486–541 (2018).
12. Seibt, T. M., Proneth, B. & Conrad, M. Role of GPX4 in ferroptosis and its pharmacological implication. *Free Radic. Biol. Med.* **133**, 144–152 (2019).
13. Bersuker, K. et al. The CoQ oxidoreductase FSP1 acts parallel to GPX4 to inhibit ferroptosis. *Nature* **575**, 688–692 (2019).
14. Doll, S. et al. FSP1 is a glutathione-independent ferroptosis suppressor. *Nature* **575**, 693–698 (2019).
15. Riegman, M., Bradbury, M. S. & Overholtzer, M. Population dynamics in cell death: mechanisms of propagation. *Trends Cancer* **5**, 558–568 (2019).
16. Yang, W. S. & Stockwell, B. R. Ferroptosis: death by lipid peroxidation. *Trends Cell Biol.* **26**, 165–176 (2016).
17. Feng, H. & Stockwell, B. R. Unsolved mysteries: how does lipid peroxidation cause ferroptosis? *PLoS Biol.* **16**, e2006203 (2018).
18. Bittker, J. A. et al. in *Probe Reports from the NIH Molecular Libraries Program* (Bethesda, MD, National Center for Biotechnology Information, 2010); <https://www.ncbi.nlm.nih.gov/books/NBK55069/>
19. Enyedi, B., Jelcic, M. & Niethammer, P. The cell nucleus serves as a mechanotransducer of tissue damage-induced inflammation. *Cell* **165**, 1160–1170 (2016).
20. Cao, J. Y. et al. A genome-wide haploid genetic screen identifies regulators of glutathione abundance and ferroptosis sensitivity. *Cell Rep.* **26**, 1544–1556 (2019).
21. Zhou, H. et al. Mechanism of radiation-induced bystander effect: role of the cyclooxygenase-2 signaling pathway. *Proc. Natl Acad. Sci. USA* **102**, 14641–14646 (2005).
22. Iyer, R., Lehnert, B. E. & Svensson, R. Factors underlying the cell growth-related bystander responses to alpha particles. *Cancer Res.* **60**, 1290–1298 (2000).
23. Chen, X. et al. Pyroptosis is driven by non-selective gasdermin-D pore and its morphology is different from MLKL channel-mediated necroptosis. *Cell Res.* **26**, 1007–1020 (2016).
24. Sborgi, L. et al. GSDMD membrane pore formation constitutes the mechanism of pyroptotic cell death. *EMBO J.* **35**, 1766–1778 (2016).
25. Wang, H. et al. Mixed lineage kinase domain-like protein MLKL causes necrotic membrane disruption upon phosphorylation by RIP3. *Mol. Cell* **54**, 133–146 (2014).
26. Zhang, Y., Chen, X., Gueydan, C. & Han, J. Plasma membrane changes during programmed cell deaths. *Cell Res.* **28**, 9–21 (2018).
27. Agmon, E., Solon, J., Bassereau, P. & Stockwell, B. R. Modeling the effects of lipid peroxidation during ferroptosis on membrane properties. *Sci. Rep.* **8**, 5155 (2018).
28. Runas, K. A., Acharya, S. J., Schmidt, J. J. & Malmstadt, N. Addition of cleaved tail fragments during lipid oxidation stabilizes membrane permeability behavior. *Langmuir* **32**, 779–786 (2016).
29. Evavold, C. L. et al. The pore-forming protein gasdermin D regulates interleukin-1 secretion from living macrophages. *Immunity* **48**, 35–44 e36 (2018).
30. Katikaneni, A. J. M., Gerlach, G., Ma, Y., Overholtzer, M. & Niethammer, P. Lipid peroxidation instructs long-range wound detection through 5-lipoxygenase in zebrafish. *Nat. Cell Biol.* (in the press).

Publisher's note Springer Nature remains neutral with regard to jurisdictional claims in published maps and institutional affiliations.

© The Author(s), under exclusive licence to Springer Nature Limited 2020

Methods

Cell culture. HT1080 cells (ATCC), HeLa cells (ATCC), HAP1 chronic myelogenous leukemia cells (the kind gift of J. Carette, Stanford School of Medicine), and MCF7 breast cancer cells (Lombardi Cancer Center, Georgetown University) were cultured in high-glucose Dulbecco's Modified Eagle's Medium (DMEM) (MSKCC Media Preparation Facility) supplemented with 10% heat-inactivated fetal bovine serum (FBS) (F2442; Sigma-Aldrich) and penicillin/streptomycin (30-002-CI; Mediatech). B16F10 melanoma cells (ATCC) and U937 promonocytic leukaemia cells (ATCC) were grown in RPMI-1640 (11875-093; Thermo Fisher) containing 10% heat-inactivated FBS and penicillin/streptomycin, and MCF10A mammary epithelium cells (ATCC) were cultured in DMEM/F12 (11320-033; Thermo Fisher) supplemented with 5% horse serum (HS) (S12150; Atlanta Biologicals), 20 ng/mL epidermal growth factor (EGF) (AF-100-15; Peprotech), 10 μ g/mL insulin (I9278; Sigma-Aldrich), 0.5 μ g/mL hydrocortisone (H-0888; Sigma-Aldrich), 100 ng/mL cholera toxin (C-8052; Sigma-Aldrich), and penicillin/streptomycin. HeLa cells expressing *Danio rerio* cytosolic phospholipase A2 (cPLA2)-mKate have been described previously¹². HAP1 cells expressing GCaMP6-NLS were generated using the Sleeping Beauty transposase system. HAP1 cells were transfected with pSB-CMV-MCS-Puro GCaMP6-NLS and pSB-cag-100x-Transposase, using Lipofectamine 3000 (L3000-015; Thermo Fisher) as recommended by the manufacturer. Amino acid-free culture medium was prepared by dialyzing FBS or HS in PBS (MSKCC Media Preparation Facility) using MWCO 3500 dialysis tubing (21-152-9; Fisherbrand) and adding it to amino acid-free base media (MSKCC Media Preparation Facility). These media were used in combination with FAC and BSO to induce ferroptosis in MCF10A and MCF7 cells, and with α MSH-tagged C' dots to induce ferroptosis in B16F10 cells.

Reagents. Ferric ammonium citrate (FAC) (F5879; Sigma-Aldrich), l-buthionine sulfoximine (BSO) (B2515; Sigma-Aldrich), and deferoxamine (DFO) (D9533; Sigma-Aldrich) were dissolved in water, and stock solutions were stored at -20°C . FAC and BSO were used at 400 μM and DFO at 200 μM . SuperKillerTRAIL (ALX-201-115-C010; Enzo) stock solution was diluted to 100 $\mu\text{g}/\text{mL}$ in KillerTRAIL dilution buffer (20 mM HEPES, 300 mM NaCl, 0.01% Tween-20, 1% sucrose, 1 mM DTT), aliquoted, and stored at -80°C . This was used at a final concentration of 50 ng/mL. Hydrogen peroxide (216763; Sigma-Aldrich) was first diluted in water and then added to cell culture media at a final concentration of 1 mM. C11-BODIPY (D3861; Molecular Probes) was dissolved in DMSO, stored at -20°C , and diluted to a final concentration of 5 μM prior to use. Sucrose (S7903; Sigma-Aldrich), raffinose (R0514; Sigma-Aldrich), polyethylene glycol (PEG) 1450 (P7181; Sigma-Aldrich), and PEG3350 (P3640; Sigma-Aldrich) were dissolved directly into cell culture media at a concentration of 20 mM. All other compounds were prepared as stock solutions in DMSO and stored at -20°C . Erastin (E7781, used at 7.5 μM with HAP1s and 2 μM with HT1080s), ferrostatin-1 (SML0583, used at 4 μM), and Trolox (238813, used at 100 μM) were from Sigma-Aldrich; RSL3 (S8155, used at 1 μM) and liproxstatin-1 (S7699, used at 200 nM) were from SelleckChem. ML162 was synthesized by Acme Bioscience (Palo Alto, CA) and was used at 4 μM . α MSH-tagged C' dots were synthesized as described previously^{8,31} in water, stored at 4°C , and used at a concentration of 15 μM . SYTOX Green (S7020; Molecular Probes) was used at a concentration of 10 nM and SYTOX Orange (S11368; Molecular Probes) at a concentration of 50 nM for all experiments.

Analysis. Single-cell time of death annotation: we used a custom MATLAB (R2016A) script to record the *xy* position and time of death (for Sytox) or time of calcium influx (for GCaMP) of each cell. All other spatiotemporal analysis (measuring propagation and statistical testing, see below) was performed in Python 3.

Measuring propagation. We used Voronoi tessellation³², a computational geometry method to divide a plane into regions given a set of loci, where each locus corresponds to a cell nucleus's *xy* location. Each point on the plane belongs to a single region, and each region consists of all the closest points to the associated nuclear locus. Neighbors were defined as regions sharing a border, which allowed us to identify all pairs of neighboring cells. Note that neighboring cells in the tessellation do not necessarily share cell-cell junctions in the experiment. For each field of view we calculated the mean difference in time of death between all neighboring cell pairs as a measure for propagation speed, marked with $\mu_{\text{exp}\Delta t}$.

Statistical test. We devised a statistical test to determine the statistical significance of the hypothesis that there is a relationship between a cell's and its neighbors' times of death. This was achieved by using a non-parametric permutation test to reject the null hypothesis that the cells' time of death is independent of their neighbors' time of death. For every field of view, the following procedure was repeated for 1,000 iterations. The recorded time of death was randomly permuted between the cells (i.e., each cell was assigned a random time of death, with the same number of deaths at each time point as in the experimental data), and the mean difference in time of death between all neighboring cell pairs was recorded. The *P* value was calculated as the fraction of iterations in which the mean time difference between neighbors using the permuted ("random") cell death was

faster than the experimental measurement. We considered a *P* value of 0.05 as statistically significant.

We devised the spatial propagation index to quantify the contribution of the spatial component to the observed experimental cell-cell propagation. This measure was defined as the deviation of the experimental mean propagation ($\mu_{\text{exp}\Delta t}$) from the 95th percentile of the mean randomly permuted death times ($\mu_{\text{perm95}\Delta t}$) normalized to $\mu_{\text{perm95}\Delta t}$: $\frac{\mu_{\text{perm95}\Delta t} - \mu_{\text{exp}\Delta t}}{\mu_{\text{perm95}\Delta t}}$. This measure can be interpreted as the fraction of the $\mu_{\text{perm95}\Delta t}$ needed to reconstruct back the spatial information in the experimental data.

Quantifying ferroptosis propagation from DIC: to quantify the distance covered by the ferroptosis wave in each field of view, lines delineating live and dead cell regions were drawn manually in NIS elements AR (Nikon, 3.22.15) at 1-h intervals, starting from a timepoint at which smaller initiation points, if present, had converged into larger waves. For each interval, the area between two lines was measured and divided by their average length to obtain the mean distance travelled during a given interval in a given field of view. Information from different fields of view in the same condition was then combined to plot the mean distance covered in each condition, and a linear regression was performed to calculate the speed of the corresponding ferroptosis wave.

Live-cell imaging. Cells were seeded on glass-bottom plates (P24G-1.5-13-F; Mattek) and treated in fresh culture media the next day. For amino acid-free conditions, cells were washed with PBS twice prior to treatment. Imaging was performed in live-cell incubation chambers maintained at 37°C and 5% CO_2 . Images were acquired every 5 to 30 min for 24–48 h using a Nikon Ti-E inverted microscope attached to a CoolSNAP charge-coupled device camera (Photometrics) and NIS Elements AR software (Nikon, 3.22.15). For experiments with ML162, time-lapse imaging was performed on plastic tissue culture plates (3527; Corning) on a Zeiss microscope using ZEN software (Zeiss). Images were quantified manually in NIS Elements AR (Nikon) or ZEN (Zeiss) and processed using ImageJ (2.0.0) and Adobe Photoshop (CS6 13.0.5).

LDH assays. LDH assays were performed using the Pierce LDH Cytotoxicity Assay Kit (88954; Thermo Fisher) following the manufacturer's instructions. Briefly, cells were seeded on 96-well plates and treated in triplicate the next day. At the indicated time, 50 μL media was transferred from each well to a well containing 50 μL assay buffer, and plates were incubated at RT for 30 min. At this point 50 μL stop solution was added to each well, bubbles were removed using a syringe, and the absorbance was read on a BioTek Synergy H1 Hybrid Reader at 490 nm and 680 nm wavelengths. The 490 nm absorbance was subtracted from the 680 nm absorbance, and background from cell culture medium was subtracted from all values. Data were averaged across technical replicates and normalized to the indicated treatment without osmoprotectants to calculate percent LDH release. For suspension cells, cells were treated in 24-well tissue culture plates containing 1 mL media per well. At the indicated time, 200 μL media was taken from each well and spun down to remove dead cells, and the supernatant was used to perform the assay as described.

Crystal violet assays. Cells were seeded on 24-well tissue culture plates (3527; Corning) and treated in triplicate the next day. After 24 h, when most control cells had died, wells were washed twice with PBS, then fixed in 4% paraformaldehyde (15710-S; Electron Microscopy Sciences) in PBS for 15 min. After washing with water, cells were stained with 0.1% crystal violet (61135; Sigma-Aldrich) in 10% ethanol for 20 min, then washed again with water until clear and allowed to air dry. After drying, crystal violet stain was dissolved in 10% acetic acid by shaking the plate at room temperature for 30 min. This solution was diluted 1:4 with water, and absorbance was measured at 590 nm on a BioTek Synergy H1 Hybrid Reader. Background absorbance from wells containing only tissue culture medium was subtracted from all readings, and values were averaged across technical replicates and normalized to the untreated controls to obtain percent viability.

Confocal imaging. Cells were plated on glass-bottom dishes and treated the next day. For C11-BODIPY^{581/591} imaging, cells were washed twice with Hank's Balanced Salt Solution (HBSS) (14025-092; Thermo Fisher) 24 h after treatment, stained in 5 μM C11-BODIPY^{581/591} in HBSS for 10 min at 37°C and 5% CO_2 , and again washed twice in HBSS. Cells were imaged at 37°C and 5% CO_2 using the UltraVIEW Vox spinning-disk confocal system (PerkinElmer) equipped with 488 nm and 568 nm lasers and an electron-multiplying charge-coupled device camera (Hamamatsu C9100-13) and attached to a Nikon Ti-E microscope. For cPLA2 imaging shown in Fig. 2f, a single confocal plane is shown from the indicated time points. For C11-BODIPY^{581/591} imaging in Extended Data Fig. 1, maximum projections are shown. Images were acquired and processed using Velocity software (PerkinElmer, version 5.2.0).

Statistics and reproducibility. Data were analyzed in Microsoft Excel (Office 2011) and GraphPad Prism 7 and are represented as mean with individual data points. *P* values were obtained using two-sided Dunnett's multiple comparisons test unless otherwise indicated. **P* < 0.05, ***P* < 0.01, ****P* < 0.001, *****P* < 0.0001. The following analyses were done using data from one experiment: spatiotemporal

analyses in Figs. 1d–h, 4b, d, e, and Extended Data Fig. 1c,e, except data for MCF7+H₂O₂ in Fig. 1g, h which was from two independent experiments. The images in Fig. 1a are representative of one experiment, and images in Fig. 2f are representative of two independent experiments. All other data were derived from three or more biologically independent experiments; exact *n* are reported in the figure legends. For LDH measurements in Figs. 3a–d and Fig. 5b, and crystal violet assay in Extended Data Fig. 1a, each experiment consisted of three technical replicates that were averaged for each condition.

Reporting Summary. Further information on research design is available in the Nature Research Reporting Summary linked to this article.

Data availability

The statistical source data that support the findings of this study have been provided as part of this publication. All other data are available from the corresponding authors upon request. Source data are provided with this paper.

Code availability

Our source code is available via GitHub at <https://github.com/AssafZaritskyLab/PropagationOfCellDeath>. This repository includes all code used to measure the mean time difference between neighboring deaths and to run the random simulations, as well as a demo dataset.

References

31. Ma, K. et al. Control of ultrasmall sub-10 nm ligand-functionalized fluorescent core–shell silica nanoparticle growth in water. *Chem. Mater.* **27**, 4119–4133 (2015).
32. Du, Q. & Gunzburger, M. Grid generation and optimization based on centroidal Voronoi tessellations. *Appl. Math. Comput.* **133**, 591–607 (2002).

Acknowledgements

This research was supported by grant 1R01GM122923 from the NIH to S.J.D. and grant CA154649 to M.O. from NCI. A.Z. was supported by the Data Science Research Center, Ben-Gurion University of the Negev, Israel. We thank members of the Overholtzer laboratory for helpful discussions.

Author contributions

M.R. and M.O. designed the study. M.R. designed, performed and analysed experiments. L.S., C.G., T.L., N.S. and A.Z. wrote the analysis code and performed computational analyses. M.R., A.Z. and M.O. wrote the paper. S.J.D., U.W., M.S.B. and P.N. provided key reagents and edited the manuscript.

Competing interests

Memorial Sloan-Kettering Cancer Center and three investigators involved in this study (M.S.B., U.W. and M.O.) have financial interests in Elucida Oncology. Research involving 'C' dots may involve one or more US or international patent applications.

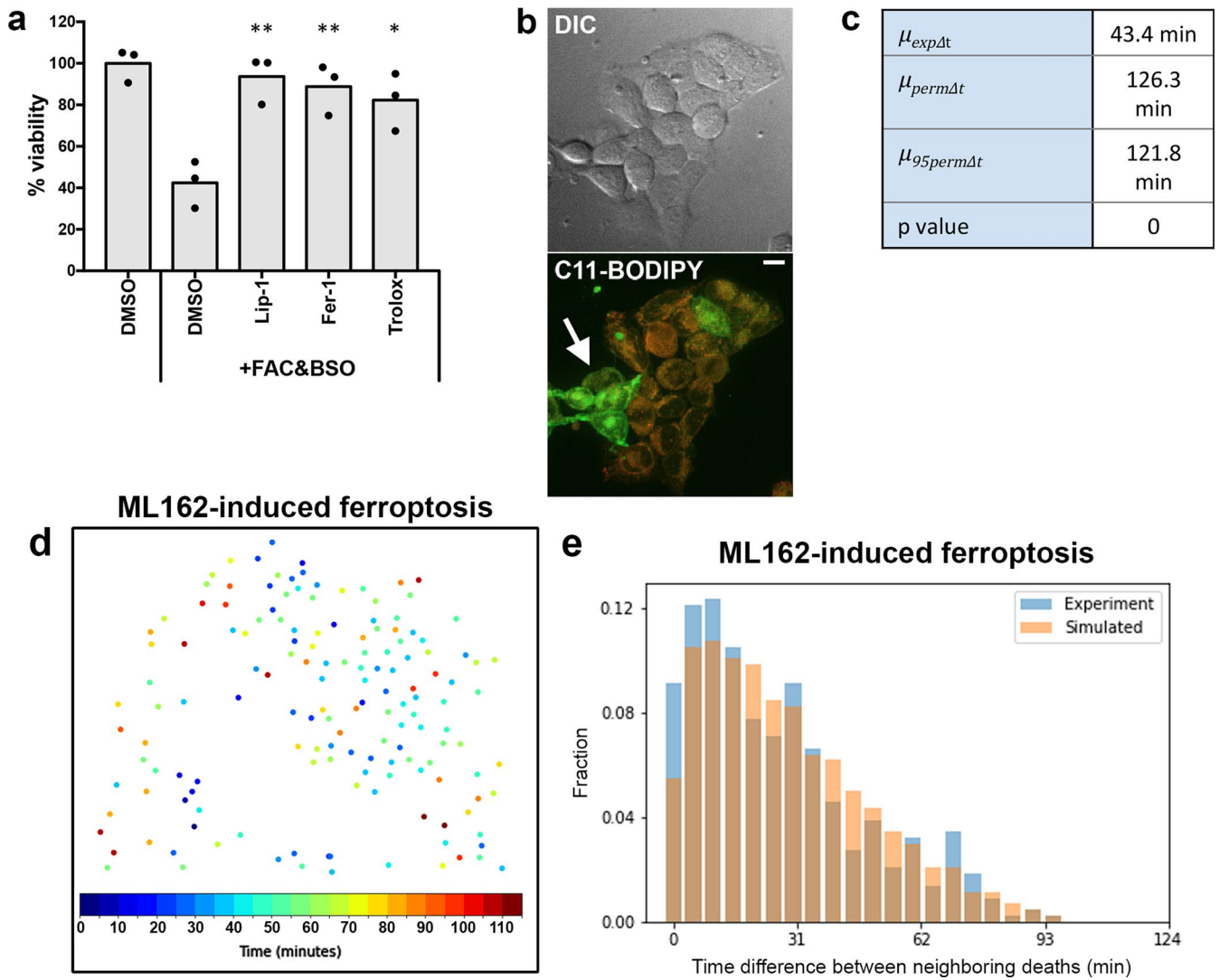
Additional information

Extended data is available for this paper at <https://doi.org/10.1038/s41556-020-0565-1>.

Supplementary information is available for this paper at <https://doi.org/10.1038/s41556-020-0565-1>.

Correspondence and requests for materials should be addressed to A.Z. or M.O.

Reprints and permissions information is available at www.nature.com/reprints.



Extended Data Fig. 1 | Treatment of cells with FAC and BSO induces ferroptosis. **a**, Viability of HAP1 cells after treatment with FAC and BSO and either DMSO or ferroptosis inhibitors as measured by crystal violet staining. $N=$ three independent experiments. Dunnett's test; $^{**}p=0.0024$ for Lip-1; $^{**}p=0.0045$ for Fer-1; $^{*}p=0.0107$ for Trolox. **b**, Confocal images of HAP1 cells treated with FAC and BSO and stained with C11-BODIPY^{581/591}. Non-oxidized probe is shown in red, oxidized probe is shown in green (arrow). Scale bar = 10 μ m. Images are representative of three independent experiments. **c**, Values from the analysis of the experiment shown in panels 1c and **d**. Note that the experimental mean time difference between neighbors ($\mu_{exp\Delta t}$) is much smaller than the mean ($\mu_{perm\Delta t}$) and 95th percentile ($\mu_{95perm\Delta t}$) obtained from the randomly permuted data. **(d)** Spatiotemporal distribution of cell death in HAP1 cells treated with ML162 to induce ferroptosis. Each dot represents a cell from a single movie representative of five fields of view from one experiment. Colors indicate relative times of cell death as determined by SYTOX Green staining. **e**, Distribution of experimental time differences between neighboring deaths in blue and averaged distribution of the corresponding permuted data in orange. Data belong to the experiment shown in panel **d** and are representative of five fields of view from one experiment. Statistical source data can be found at Source data Extended Data Fig. 1.

Reporting Summary

Nature Research wishes to improve the reproducibility of the work that we publish. This form provides structure for consistency and transparency in reporting. For further information on Nature Research policies, see [Authors & Referees](#) and the [Editorial Policy Checklist](#).

Statistics

For all statistical analyses, confirm that the following items are present in the figure legend, table legend, main text, or Methods section.

n/a Confirmed

- | | | |
|-------------------------------------|-------------------------------------|--|
| <input type="checkbox"/> | <input checked="" type="checkbox"/> | The exact sample size (n) for each experimental group/condition, given as a discrete number and unit of measurement |
| <input type="checkbox"/> | <input checked="" type="checkbox"/> | A statement on whether measurements were taken from distinct samples or whether the same sample was measured repeatedly |
| <input type="checkbox"/> | <input checked="" type="checkbox"/> | The statistical test(s) used AND whether they are one- or two-sided
<i>Only common tests should be described solely by name; describe more complex techniques in the Methods section.</i> |
| <input checked="" type="checkbox"/> | <input type="checkbox"/> | A description of all covariates tested |
| <input type="checkbox"/> | <input checked="" type="checkbox"/> | A description of any assumptions or corrections, such as tests of normality and adjustment for multiple comparisons |
| <input type="checkbox"/> | <input checked="" type="checkbox"/> | A full description of the statistical parameters including central tendency (e.g. means) or other basic estimates (e.g. regression coefficient) AND variation (e.g. standard deviation) or associated estimates of uncertainty (e.g. confidence intervals) |
| <input type="checkbox"/> | <input checked="" type="checkbox"/> | For null hypothesis testing, the test statistic (e.g. F , t , r) with confidence intervals, effect sizes, degrees of freedom and P value noted
<i>Give P values as exact values whenever suitable.</i> |
| <input checked="" type="checkbox"/> | <input type="checkbox"/> | For Bayesian analysis, information on the choice of priors and Markov chain Monte Carlo settings |
| <input checked="" type="checkbox"/> | <input type="checkbox"/> | For hierarchical and complex designs, identification of the appropriate level for tests and full reporting of outcomes |
| <input checked="" type="checkbox"/> | <input type="checkbox"/> | Estimates of effect sizes (e.g. Cohen's d , Pearson's r), indicating how they were calculated |

Our web collection on [statistics for biologists](#) contains articles on many of the points above.

Software and code

Policy information about [availability of computer code](#)

Data collection

Data were collected using NIS Elements AR (3.22.15), Volocity (5.2.0), and ZEN (Zeiss) software

Data analysis

Data were processed and analyzed using NIS elements AR (3.22.15), ImageJ (2.0.0), GraphPad Prism 7, Microsoft Excel (Office 2011), Adobe Photoshop (CS6 13.0.5), MATLAB (R2016a) and Python 3. Custom scripts are available at <https://github.com/AssafZaritskyLab/PropagationOfCellDeath>

For manuscripts utilizing custom algorithms or software that are central to the research but not yet described in published literature, software must be made available to editors/reviewers. We strongly encourage code deposition in a community repository (e.g. GitHub). See the Nature Research [guidelines for submitting code & software](#) for further information.

Data

Policy information about [availability of data](#)

All manuscripts must include a [data availability statement](#). This statement should provide the following information, where applicable:

- Accession codes, unique identifiers, or web links for publicly available datasets
- A list of figures that have associated raw data
- A description of any restrictions on data availability

The statistical source data that support the findings of this study have been provided as part of this publication. All other data are available from the corresponding authors upon request.

Field-specific reporting

Please select the one below that is the best fit for your research. If you are not sure, read the appropriate sections before making your selection.

- Life sciences Behavioural & social sciences Ecological, evolutionary & environmental sciences

For a reference copy of the document with all sections, see [nature.com/documents/nr-reporting-summary-flat.pdf](https://www.nature.com/documents/nr-reporting-summary-flat.pdf)

Life sciences study design

All studies must disclose on these points even when the disclosure is negative.

- Sample size
- Data exclusions
- Replication
- Randomization
- Blinding

Reporting for specific materials, systems and methods

We require information from authors about some types of materials, experimental systems and methods used in many studies. Here, indicate whether each material, system or method listed is relevant to your study. If you are not sure if a list item applies to your research, read the appropriate section before selecting a response.

Materials & experimental systems

- | | |
|-------------------------------------|---|
| n/a | Involvement in the study |
| <input checked="" type="checkbox"/> | <input type="checkbox"/> Antibodies |
| <input type="checkbox"/> | <input checked="" type="checkbox"/> Eukaryotic cell lines |
| <input checked="" type="checkbox"/> | <input type="checkbox"/> Palaeontology |
| <input checked="" type="checkbox"/> | <input type="checkbox"/> Animals and other organisms |
| <input checked="" type="checkbox"/> | <input type="checkbox"/> Human research participants |
| <input checked="" type="checkbox"/> | <input type="checkbox"/> Clinical data |

Methods

- | | |
|-------------------------------------|---|
| n/a | Involvement in the study |
| <input checked="" type="checkbox"/> | <input type="checkbox"/> ChIP-seq |
| <input checked="" type="checkbox"/> | <input type="checkbox"/> Flow cytometry |
| <input checked="" type="checkbox"/> | <input type="checkbox"/> MRI-based neuroimaging |

Eukaryotic cell lines

Policy information about [cell lines](#)

- Cell line source(s)
- Authentication
- Mycoplasma contamination
- Commonly misidentified lines (See [ICLAC](#) register)